**Steel and Composite Structures**, *Vol. 17, No. 3 (2014) 287-303*
DOI: http://dx.doi.org/10.12989/scs.2014.17.3.287 

# Experimental study on hysteretic properties of SRC columns with high steel ratio

Xilin Lu [1], Xiaowei Yin [*2] and Huanjun Jiang [1]

[1] *State Key laboratory of Disaster Reduction in Civil Engineering, Tongji University, Shanghai, China*
[2] *China Academy of Building Research, Beijing, China*

(*Received November 27, 2012, Revised October 01, 2013, Accepted February 28, 2014*)

**Abstract.** 8 steel reinforced concrete (SRC) columns with the encased steel ratio of 13.12% and 15.04% respectively were tested under the test axial load ratio of 0.33-0.80 and the low-frequency cyclic lateral loading. The cross sectional area of composite columns was 500 mm × 500 mm. The mechanical properties, failure modes and deformabilities were studied. All the specimens produced flexure failure subject to combined axial force, bending moment and shear. Force-displacement hysteretic curves, strain curves of encased steels and rebars were obtained. The interaction behavior of encased steel and concrete were verified. The hysteretic curves of columns were plump in shapes. Hysteresis loops were almost coincident under the same levels of lateral loading, and bearing capacities did not change much, which indicated that the columns had good energy-dissipation performance and seismic capacity. Based on the equilibrium equation, the suggested practical calculation method could accurately predict the flexural strength of SRC columns with cross-shaped section encased steel. The obtained *M-N* curves of SRC columns can be used as references for further studies.

**Keywords:** axial load ratio; cyclic loading test; flexural strength; high ratio of encased steel; SRC

## 1. Introduction

Steel reinforced concrete (SRC) columns with high ratio of encased steel have been widely used in major projects because of its excellent bearing capacity, good energy dissipation, and ductility and so on. In China, the landmark buildings such as the New CCTV Building, the China World Trade Center Phase III in Beijing, and Qsingdao Wanbang Center, etc. have been employed SRC columns whose encased steel ratio are higher than 15% as the load-carrying components. In the past twenty years, researchers had carried out a great deal of tests on the seismic behaviors of SRC columns. Chen *et al*. (2005) conducted an experimental research to investigate the behavior of concrete-encased composite beam-columns with T-shaped steel sections under the lateral cyclic loading and the axial compression. Sav *et al*. (2011) studied the strong points and weak points of composite columns with high strength concrete and normal strength concrete respectively. Mirza *et al*. (1996) studied the second-order effects composite steel-concrete beam-columns based on 16 specimens. However, the encased steel ratios of those test specimens were mostly less than 10%

*Corresponding author, Ph.D., E-mail: yxwtoo567@163.com


http://www.techno-press.org/?journal=scs&subpage=8 ISSN: 1229-9367 (Print), 1598-6233 (Online)

(Wang 1999, Plumier and Doneux 2001, Weng *et al*. 2008, Zheng *et al*. 2012). Tests on higher encased steel ratio columns, especially those between 10%-15% and even higher, were fairly scarce (Elghazouli and Dowling 1992, Boyd *et al*. 1995, Hajjar 2002, Zhang *et al*. 2012).

In paper, 8 concrete-encased cross-shaped steel composite columns with 13.12% and 15.04% of encased steel ratio were tested under the low-frequency, the cyclic lateral loading and the constant axial compressive load. The flexural strength of SRC column is studied.

## 2. Experimental program

### *2.1 Test specimens*

A total of 8 specimens were designed. The test specimens had a square cross section of 500 mm × 500 mm. Fig. 1 shows the configurations of the cross sections and the sizes of encased steel. The test specimens consisted of structural steel shapes, longitudinal reinforcements, transverse reinforcements, and concrete. Encased steel with cross-shaped steel section was adopted, since it was generally used in the inner columns of composite buildings. The variables studied in this

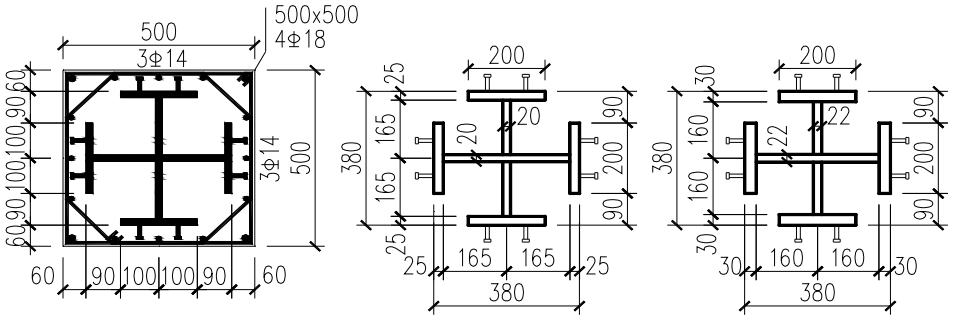


Fig. 1 Dimension details of cross-section

Table 1 Summary of test specimens

| Number | Specimen designation | $\rho_a$ *% | Transverse reinforcement | $\lambda_v$ /% | $\rho_v$ /% | $n$ | $n_t$ | $N_t$/kN |
|---|---|---|---|---|---|---|---|---|
| 1 | 13S10N10 | 13.12 | Φ8+Φ10@100 | 11.61 | 1.04 | 1.0 | 0.66 | 11634 |
| 2 | 13S14N05 | 13.12 | Φ12+Φ8@100 | 15.32 | 1.37 | 0.5 | 0.33 | 5817 |
| 3 | 15S10N07 | 15.04 | Φ8+Φ10@100 | 11.61 | 1.04 | 0.7 | 0.47 | 9005 |
| 4 | 15S10N10 | 15.04 | Φ8+Φ10@100 | 11.61 | 1.04 | 1.0 | 0.67 | 12864 |
| 5 | 15S14N05 | 15.04 | Φ12+Φ8@100 | 15.32 | 1.37 | 0.5 | 0.34 | 6432 |
| 6 | 15S14N07 | 15.04 | Φ12+Φ8@100 | 15.32 | 1.37 | 0.7 | 0.47 | 9005 |
| 7 | 15S14N10 | 15.04 | Φ12+Φ8@100 | 15.32 | 1.37 | 1.0 | 0.67 | 12864 |
| 8 | 15S19N12 | 15.04 | Φ12+Φ12@100 | 20.69 | 1.85 | 1.2 | 0.80 | 15437 |

$\rho_a$*: ratio of encased steel;
$\lambda_v$: transverse reinforcement characteristic value;
$\rho_v$: ratio of transverse reinforcement

paper included the axial load ratio, the ratio of encased steel, and the transverse reinforcement ratio. Table 1 summarizes the test specimens. Each specimen is numbered to reflect its variables. For instance, in specimen 13S10N10, 13 represents the encased steel ratio is 13.12% which is defined as the percentage of the area of encased steel in total cross sectional area; the subsequent figure 10, indicates the transverse reinforcement ratio which is defined as the percentage of volume of transverse reinforcement in each unit volume of the core concrete which is surrounded by transverse reinforcement; the third figure 10 represents the design axial load ratio is 1.0.

In this paper, the design axial load ratio is defined as

$$n \approx \frac{1.2N_t}{f_{ck}A_c/1.4 + f_{ak}A_a/1.1} \tag{1}$$

The test axial load ratio in Table 1 is defined as

$$n_t = \frac{N_t}{f_{ck}A_c + f_{ak}A_a} \tag{2}$$

where $N_t$ is the applied axial compressive load; $f_{ck}$ and $f_{ak}$ are the standard strengths of concrete and steel shaped respectively according to Chinese concrete code (2010); $A_c$ and $A_a$ are the cross sectional area of concrete and encased steel respectively.

Another analysis parameter, the transverse reinforcement characteristic value, is expressed as follows according to Chinese concrete code

$$\lambda_v = \rho_v \frac{f_{yv}}{f_{ck}} \tag{3}$$

where $f_{yv}$ is the tension yield strength of the transverse reinforcement.

As is shown in Fig. 1, a longitudinal bar of 18 mm diameter is placed at each corner of the column, while three longitudinal bars of 14 mm diameter are located in each edge. Transverse reinforcement group consists of two levels, one is the outer hoop in square shape, and the other one was the inner hoop in octagonal shape. In Table 1, for the instance, ⌀8+⌀10@100 represents the outer square hoop using the transverse reinforcements of 8 mm diameter, and the inner octagonal hoop using bars of 10 mm diameter, while the hoop spacing is 100 mm. All the bars are HRB335, with yield strengths varying in the range of 368-377 MPa. The concrete cube strength is 50 MPa at 28 days, and prism strength is 33 MPa which is approximately adopted as $f_{ck}$. Measured mechanical properties of structural steel are shown in Table 2.

In order to keep encased steel and concrete work cooperatively, and to prevent the shear bonding failure in the material interface, two stud connectors were fixed in each flange in 100 mm intervals in the vertical and horizontal directions as shown in Fig. 1. The base of the specimen

Table 2 Measured mechanical properties of structural steel and reinforcement

| Thickness of steel plate | 20 mm | 22 mm | 25 mm | 30 mm |
|---|---|---|---|---|
| Yield strength $f_{ak}$ (MPa) | 294 | 295 | 348 | 333 |
| Ultimate strength (MPa) | 447 | 464 | 472 | 477 |

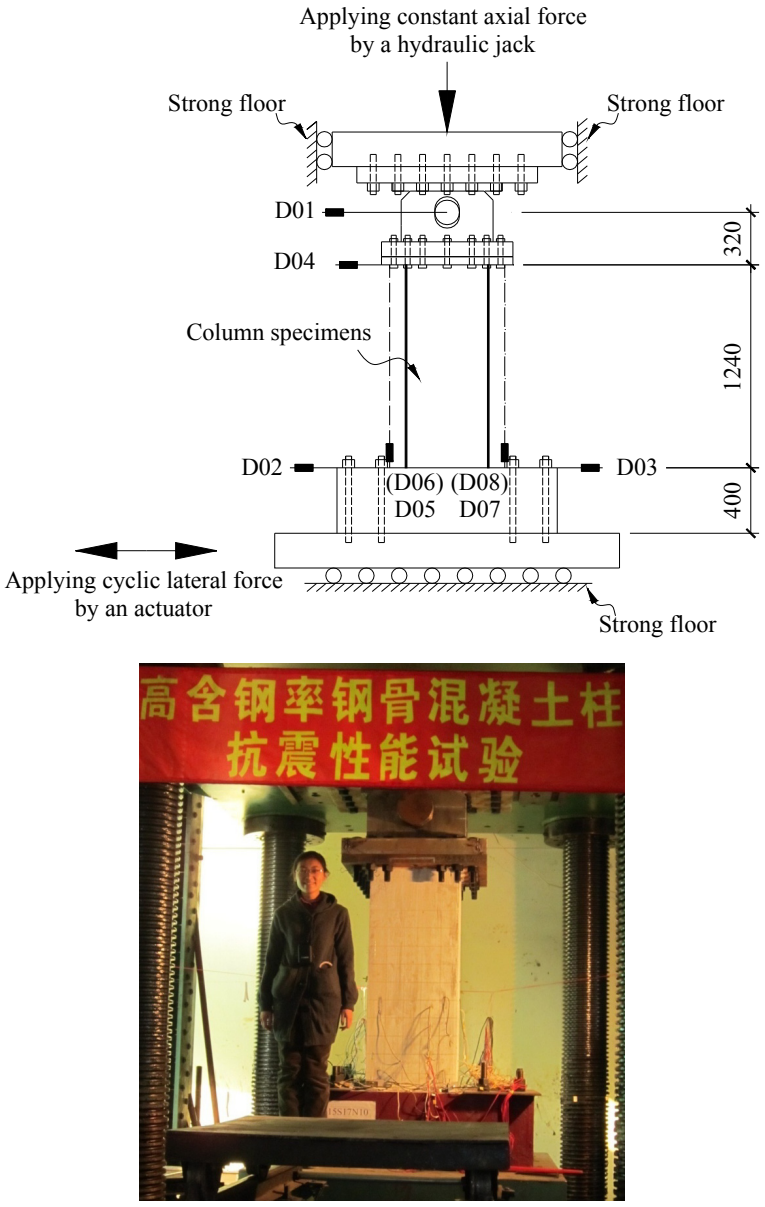


Fig. 2 Test setup

was assumed as perfect rigid, employing a concrete-filled rectangular steel tube with encased steel diaphragms inside.

### *2.2 Test setup and test procedure*

Tests were conducted in the State Key Laboratory of Disaster Reduction in Civil Engineering (SKLDRCE), Tongji University, Shanghai, China. All the specimens were loaded under a constant

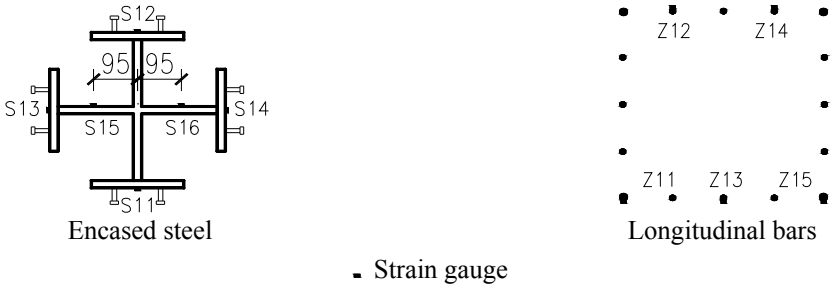


Fig. 3 Arrangement of strain gauges

axial load then subjected to a cyclic lateral force. The test setup is shown in Fig. 2. A ball joint was fixed in the experiment machine, connecting the top of the specimen to the upper loading table. The bottom of the column was fixed to the lower loading table.

The ball joint ensured that the top of the column rotate freely in the test process. When testing, the axial load was exerted through the upper loading table of the experiment machine, and then the lateral load was applied by a hydraulic actuator to the bottom of the column by using a displacement-controlled testing. With the above setup, the distribution of the bending moment in the specimen was similar to that in a prototype column between the point with maximum bending moment and inflection point when the column was subjected to a lateral load. The loading cycles terminated when the lateral load dropped to 85% of the maximum bearing capacity.

In the tests, the following instrumentations were employed as illustrated in Figs. 2 and 3: (a) 4 LVDTs (D05-D08) detected the vertical deformations of the specimens; (b) 2 LVDTs (D02, D03) were employed in order to measure the bottom lateral displacement; (c) 1 LVDT (D01) was utilized to measure the horizontal displacement of the ball joint; (d) a series of strain gauges were installed to monitor deformations of the encased steel and longitudinal bars.

## 3. Experimental results and discussion

### *3.1 Experimental phenomena*

The two sides parallel to the displacement direction were defined as positive side and negative side, respectively.

The axial load ratios of specimens13S14N05, 15S10N07, 15S14N05 and 15S14N07 were relatively low. When the lateral displacement reached 20%~25% yielding displacement, horizontal cracks occurred at the bottom of the tensile zone. Then horizontal cracks developed to the positive and negative sides. With the lateral displacement increased, vertical cracks were observed at the bottom of the compression zone. The number of horizontal cracks at the tensile zone continued to rise and transformed into inclined cracks when they extend to the positive and negative sides. Inclined cracks crossed with each other in the two sides. After the maximum strength load, spalling of the concrete occurred. The longitudinal bars revealed. In the strength degradation stage, longitudinal bars at the tensile zone were broken. The height of the column decreased obviously. The lateral load dropped rapidly after the longitudinal bars buckled

Specimens 13S10N10, 15S10N10 and 15S14N10 had a relative large axial load ratio. Under


(a) 15S17N05


(b) 15S17N07

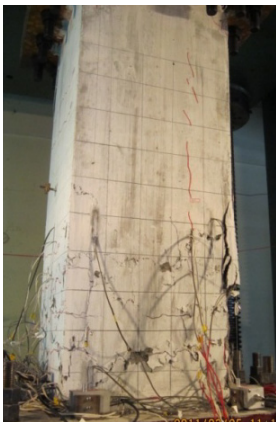
(c) 15S17N10

Fig. 4 Appearance of specimens when inter-storey drift angle reached 1/50

the cyclic lateral force, first of all, vertical cracks appeared at the corner of the bottom of the column in the compression zone. When the lateral displacement reached 15%~25% yielding displacement, the horizontal cracks appeared in the tensile side. With the increasing of the lateral displacement, the horizontal cracks developed to the positive and negative sides. The inclined and vertical cracks were observed at the bottom of the specimens. Part of the horizontal cracks changed their developing directions and became inclined cracks. When approached the maximum strength load, the cracks accelerated developed. The number of cracks in all sides increased dramatically. After the maximum strength load, gradually spalling of concrete occurred. The longitudinal bars and stirrups revealed. Then larger pieces of concrete shucked off. Longitudinal bars were broken in the tensile zone. The height of column decreased obviously.

The test axial load ratio of specimens 15S19N12 was 0.8. Under the lateral force, the vertical cracks formed in the compression zone when the lateral displacement was about 15% yielding displacement. Then the horizontal cracks appeared at the bottom of the tensile zone. In the positive side, the diagonal cracks at the bottom of the specimens turned into the horizontal cracks, and developed. When the lateral displacement was about 65% yielding displacement, the diagonal cracks were observed in the middle of the positive side, and then extended inclined to the edge. During the yielding and the maximum strength displacement, the number of cracks in all sides increased dramatically. After the maximum strength load, the concrete cover was spalled, and a large number of the vertical cracks appeared. Then the concrete was seriously broken. Crushing of the concrete was followed by local buckling of the longitudinal bars.

Fig. 4 shows the appearance of the specimens when the inter-storey drift angle reacheed 1/50.

### *3.2 Characteristics of lateral load-displacement curves*

The seismic response of the specimens is presented in the lateral load-displacement hysteresis curves. Fig. 5 shows the lateral load-displacement hysteretic curve of specimens. The horizontal axis represents the lateral displacement and the vertical axis is the lateral load. As indicated in Fig. 5, all the specimens demonstrated good energy dissipation capacity under the cyclic loading. The hysteretic curves of columns were plump in shapes. Hysteresis loops were almost coincident, and

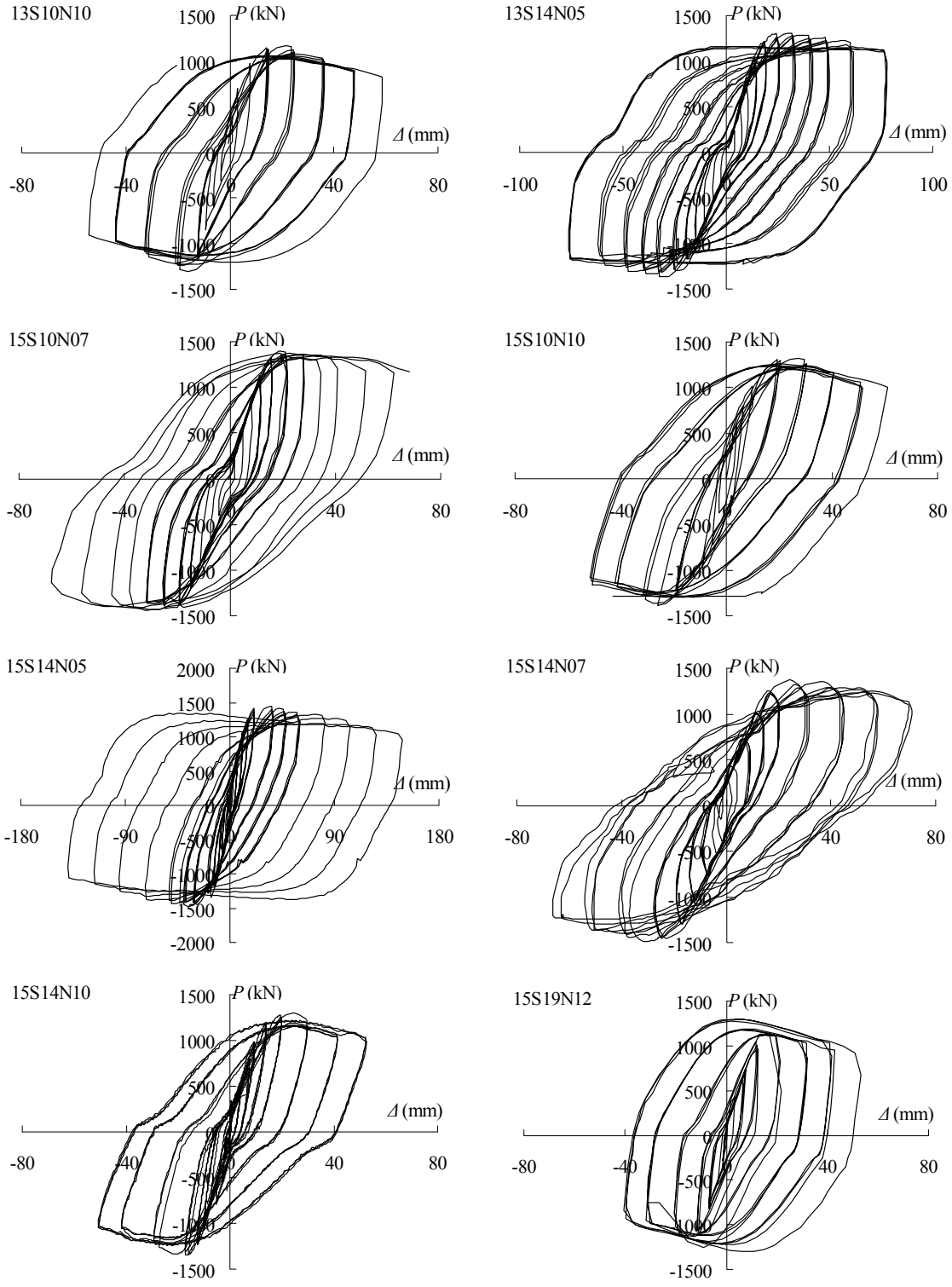


Fig. 5 Force-displacement hysteretic curve of specimens

bearing capacities were not obvious decreased under the same levels of lateral loading.

However, the hysteresis curves were highly affected by the level of the axial load ratio. Specimens with the large axial load ratio showed relatively worse cyclic performance than those with the low axial load ratio. The specimens with the low axial load ratio demonstrated much more energy absorption capacity.

When the cross section of the columns was subjected to bending moment, the internal compressive force could be resisted by the encased steel, with little contribution from the much less longitudinal bars, in addition to the concrete. Moreover, the encased steel section could substantially confine the concrete core in the compression zone. Meanwhile, the longitudinal bars and the encased steel in the tensile zone could provide the corresponding tensile force. Therefore, the hysteresis curves of the columns under cyclic loading were very stable, especially demonstrated in the specimens with the low axial load. Slight strength degradation was observed due to the minor crushing of the concrete. Besides, the concrete cover in the compression zone was prone to crush. The strength and stiffness of the column were deteriorated due to the crushing and spalling of the concrete cover and subsequent buckling of the longitudinal bars (Chen *et al*. 2005). The behavior of the specimens with 1.2 of the axial load ratios was somewhat similar to that of a steel column.

### *3.3 Ductility factor and maximum strength*

Displacement ductility factor is defined as the ratio of the displacement corresponding to 15% drop in the strength from the maximum value to the yielding displacement. The yielding point is defined as where the secant line connecting the origin and the 60% maximum load point in the ascent stage intersects the tangent line of the maximum load point. The main experimental results for all specimens under the constant axial compression are presented in Table 3. In Table 3, the values are averaged over the positive and negative directions. The effect of the axial load ratio can be seen from the comparison of specimens in 15S10N07, 15S10N10 series and 15S14N05, 15S14N07, 15S14N10 series. The small axial load ratio can effectively lead to higher maximum

Table 3 Details of test results

| Number | Specimen designation | $P_y^*$ (kN) | $\Delta_y$ (mm) | $P_{max}$ (kN) | $\Delta_{pmax}$ (mm) | $P_u$ (kN) | $\Delta_u$ (mm) | $\mu$ |
|---|---|---|---|---|---|---|---|---|
| 1 | 13S10N10 | 983 | 9.6 | 1210 | 17.2 | 1029 | 40.7 | 4.3 |
| 2 | 13S14N05 | 1232 | 15.1 | 1335 | 30.0 | 1135 | 78.0 | 5.2 |
| 3 | 15S10N07 | 1219 | 13.2 | 1409 | 24.7 | 1198 | 67.4 | 5.1 |
| 4 | 15S10N10 | 1084 | 10.8 | 1352 | 22.5 | 1149 | 50.0 | 4.6 |
| 5 | 15S14N05 | 1310 | 13.9 | 1470 | 33.5 | 1249 | 93.5 | 6.7 |
| 6 | 15S14N07 | 1230 | 13.0 | 1423 | 29.0 | 1209 | 66.5 | 5.1 |
| 7 | 15S14N10 | 1077 | 10.3 | 1331 | 20.6 | 1131 | 47.4 | 4.6 |
| 8 | 15S19N12 | 1063 | 10.0 | 1214 | 18.6 | 1032 | 39.6 | 4.0 |

$P_y^*$: yielding strength; $\Delta_y$: yielding displacement; $P_{max}$: maximum strength;
$\Delta_{pmax}$: maximum strength displacement: displacement corresponding to $P_{max}$;
$P_u$: residual strength: strength corresponding to 15% drop from $P_{max}$;
$\Delta_u$: residual strength displacement: displacement corresponding to $P_u$; $\mu$: displacement ductility factor.

strength and large deformation capacity. Therefore, for instance, the specimen 15S14N05, with the low axial load, can increase the maximum strength and displacement ductility factor more than the specimen 15S14N07 and 15S14N10. Due to the higher encased steel ratio, obvious increases of the maximum strength and displacement ductility capacity were observed for specimens with encased steel ratio of 15.04% compared to those with 13.12%.

### *3.4 Distribution of strain*

In the tests, a series of strain gauges were installed in the encased steel and longitudinal bars at the cross section which was 80 mm far from the top of the base. Fig. 6 shows the strain distribution of encased steel and longitudinal bars along the height of the cross section of specimens 15S14N05 and 15S14N10. In the figure, the horizontal axis represents the strain and the vertical axis is the distance from the symmetry axis of the cross section and the measured point. The strain distributions are shown as the loading displacements were 3 mm, 5 mm, 8 mm, 10 mm and 12 mm.

To calculate the flexural strength, plane sections were assumed to remain the plane based on the assumption of the full composite action up to failure between the different components of the column. As shown in the Fig. 6, the strain distributions of the encased steel and longitudinal bars

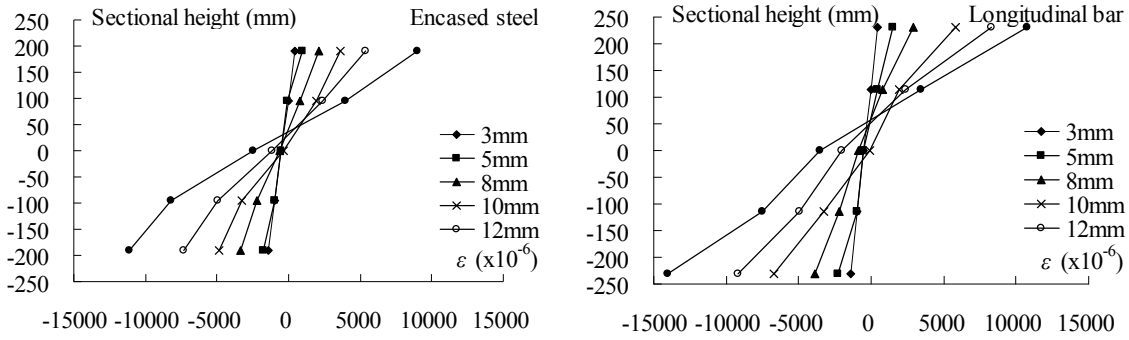


(a) 15S14N05

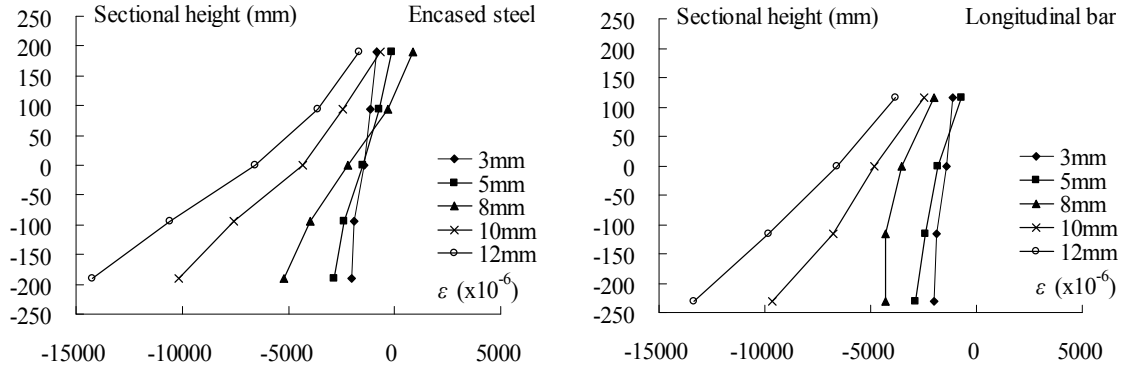


(b) 15S14N10

Fig. 6 Strain distribution of encased steel and longitudinal bar

agreed with the assumption of plane section.

## 4. Calculation of the flexural strength

### 4.1 Calculation assumption

The following assumptions are adopted when calculating the flexural strength for eccentric compression member.

(1) The strain of section is assumed to remain plane up to failure.
(2) The relative slips between bars, encased steel and concrete are ignored.
(3) The tension capacity of concrete is ignored.
(4) The stress diagram of the concrete compression zone of the normal section is simplified by an equivalent rectangular stress diagram.

The calculation of the flexural strength proposed in this paper derived from limit equilibrium theory; stress of web and the flanges of encased steel are simplified to the rectangle stress diagrams.

For different strain distribution conditions, the corresponding calculational expressions of the flexural and axial compressive strength of the web and the flanges of encased steel are proposed. There are five cases to consider, based on the possible locations of the neutral axis.

The eccentric compressive strength of the concrete-encased cross-shaped steel composite column can be calculated as follows

$$N \le \alpha_1 f_c b x + f'_y A'_s + f'_a A'_{af} - \sigma_s A_s - \sigma_a A_{af} + N_{aw} \tag{4}$$

$$M \le \alpha_1 f_c b x\left(h_0 - \frac{x}{2}\right) + f'_y A'_s\left(h_0 - a'_s\right) + f'_a A'_{af}\left(h_0 - a'_a\right) + N\left(\frac{h}{2} - h_0\right) + M_{aw} \tag{5}$$

in which

$$\left.\begin{aligned} N_{aw} &= N_{aw1} + N_{aw2} + N_{aw3} \\ M_{aw} &= M_{aw1} + M_{aw2} + M_{aw3} \end{aligned}\right\} \tag{6}$$

(1) when $\delta_3 h_0 < \dfrac{x}{\beta_1} < \delta_5 h_0$

$$\left.\begin{aligned} N_{aw1} &= \left[\frac{2\xi}{\beta_1} - \left(\delta_1 + \delta_2\right)\right] t_w h_0 f_a \\ N_{aw2} &= 2\left[\frac{2\xi}{\beta_1} - \left(\delta_3 + \delta_4\right)\right] t'_f h_0 f_a \\ N_{aw3} &= -\left(\delta_6 - \delta_5\right)\left(h'_w - t_w\right) h_0 f_a \end{aligned}\right\} \tag{7}$$

$$\left.\begin{aligned} M_{aw1} &= \left[0.5\left(\delta_1^2+\delta_2^2\right)-\left(\delta_1+\delta_2\right)+2\frac{\xi}{\beta_1}-\left(\frac{\xi}{\beta_1}\right)^2\right]t_w h_0^2 f_a \\ M_{aw2} &= 2\left[0.5\left(\delta_3^2+\delta_4^2\right)-\left(\delta_3+\delta_4\right)+2\frac{\xi}{\beta_1}-\left(\frac{\xi}{\beta_1}\right)^2\right]t'_f h_0^2 f_a \\ M_{aw3} &= -\left[0.5\left(\delta_5^2-\delta_6^2\right)+\left(\delta_6-\delta_5\right)\right]\left(h'_w-t_w\right)h_0^2 f_a \end{aligned}\right\} \tag{8}$$

(2) when $\delta_5 h_0 < \dfrac{x}{\beta_1} < \delta_6 h_0$

$$\left.\begin{aligned} N_{aw1} &= \left[\frac{2\xi}{\beta_1}-\left(\delta_1+\delta_2\right)\right]t_w h_0 f_a \\ N_{aw2} &= 2\left[\frac{2\xi}{\beta_1}-\left(\delta_3+\delta_4\right)\right]t'_f h_0 f_a \\ N_{aw3} &= -\left[\frac{2\xi}{\beta_1}-\left(\delta_5+\delta_6\right)\right]\left(h'_w-t_w\right)h_0 f_a \end{aligned}\right\} \tag{9}$$

$$\left.\begin{aligned} M_{aw1} &= \left[0.5\left(\delta_1^2+\delta_2^2\right)-\left(\delta_1+\delta_2\right)+2\frac{\xi}{\beta_1}-\left(\frac{\xi}{\beta_1}\right)^2\right]t_w h_0^2 f_a \\ M_{aw2} &= 2\left[0.5\left(\delta_3^2+\delta_4^2\right)-\left(\delta_3+\delta_4\right)+2\frac{\xi}{\beta_1}-\left(\frac{\xi}{\beta_1}\right)^2\right]t'_f h_0^2 f_a \\ M_{aw3} &= \left[0.5\left(\delta_5^2+\delta_6^2\right)-\left(\delta_5+\delta_6\right)+2\frac{\xi}{\beta_1}-\left(\frac{\xi}{\beta_1}\right)^2\right]\left(h'_w-t_w\right)h_0^2 f_a \end{aligned}\right\} \tag{10}$$

(3) when $\delta_6 h_0 < \dfrac{x}{\beta_1} < \delta_4 h_0$

$$\left.\begin{aligned} N_{aw1} &= \left[\frac{2\xi}{\beta_1}-\left(\delta_1+\delta_2\right)\right]t_w h_0 f_a \\ N_{aw2} &= 2\left[\frac{2\xi}{\beta_1}-\left(\delta_3+\delta_4\right)\right]t'_f h_0 f_a \\ N_{aw3} &= \left(\delta_6-\delta_5\right)\left(h'_w-t_w\right)h_0 f_a \end{aligned}\right\} \tag{11}$$

$$\left.\begin{aligned} M_{aw1} &= \left[0.5\left(\delta_1^2+\delta_2^2\right)-\left(\delta_1+\delta_2\right)+2\frac{\xi}{\beta_1}-\left(\frac{\xi}{\beta_1}\right)^2\right]t_w h_0^2 f_a \\ M_{aw2} &= 2\left[0.5\left(\delta_3^2+\delta_4^2\right)-\left(\delta_3+\delta_4\right)+2\frac{\xi}{\beta_1}-\left(\frac{\xi}{\beta_1}\right)^2\right]t'_f h_0^2 f_a \\ M_{aw3} &= -\left[0.5\left(\delta_5^2-\delta_6^2\right)+\left(\delta_6-\delta_5\right)\right]\left(h'_w-t_w\right)h_0^2 f_a \end{aligned}\right\} \tag{12}$$

(4) when $\delta_4 h_0 < \dfrac{x}{\beta_1} < \delta_2 h_0$

$$\left.\begin{aligned} N_{aw1} &= \left[\frac{2\xi}{\beta_1}-\left(\delta_1+\delta_2\right)\right]t_w h_0 f_a \\ N_{aw2} &= 2\left(\delta_4-\delta_3\right)t'_f h_0 f_a \\ N_{aw3} &= \left(\delta_6-\delta_5\right)\left(h'_w-t_w\right)h_0 f_a \end{aligned}\right\} \tag{13}$$

$$\left.\begin{aligned} M_{aw1} &= \left[0.5\left(\delta_1^2+\delta_2^2\right)-\left(\delta_1+\delta_2\right)+2\frac{\xi}{\beta_1}-\left(\frac{\xi}{\beta_1}\right)^2\right]t_w h_0^2 f_a \\ M_{aw2} &= 2\left[0.5\left(\delta_3^2-\delta_4^2\right)+\left(\delta_4-\delta_3\right)\right]t'_f h_0^2 f_a \\ M_{aw3} &= \left[0.5\left(\delta_5^2-\delta_6^2\right)+\left(\delta_6-\delta_5\right)\right]\left(h'_w-t_w\right)h_0^2 f_a \end{aligned}\right\} \tag{14}$$

(5) when $\delta_2 h_0 < \dfrac{x}{\beta_1}$

$$\left.\begin{aligned} N_{aw1} &= \left(\delta_2-\delta_1\right)t_w h_0 f_a \\ N_{aw2} &= 2\left(\delta_4-\delta_3\right)t'_f h_0 f_a \\ N_{aw3} &= \left(\delta_6-\delta_5\right)\left(h'_w-t_w\right)h_0 f_a \end{aligned}\right\} \tag{15}$$

$$\left.\begin{aligned} M_{aw1} &= \left[0.5\left(\delta_1^2-\delta_2^2\right)+\left(\delta_2-\delta_1\right)\right]t_w h_0^2 f_a \\ M_{aw2} &= 2\left[0.5\left(\delta_3^2-\delta_4^2\right)+\left(\delta_4-\delta_3\right)\right]t'_f h_0^2 f_a \\ M_{aw3} &= \left[0.5\left(\delta_5^2-\delta_6^2\right)+\left(\delta_6-\delta_5\right)\right]\left(h'_w-t_w\right)h_0^2 f_a \end{aligned}\right\} \tag{16}$$

The stress of longitudinal bars $\sigma_s$ and the stress of flange $\sigma_a$ in the tensile zone can be calculated as:

(1) when $x \le \xi_b h_0$, $\sigma_s = f_y$, $\sigma_a = f_a$;

(2) when $x \le \xi_b h_0$, $\sigma_s = \frac{f_y}{\xi_b - \beta_1}\left(\frac{x}{h_0} - \beta_1\right)$, $\sigma_a = \frac{f_a}{\xi_b - \beta_1}\left(\frac{x}{h_0} - \beta_1\right)$;

where

$N$ – the applied or the design axial compressive load;

$M$ – the normal section flexural strength;

$\alpha_1$, $\beta_1$ – coefficients. according to "Code for design of concrete structures" (2010) of China, when the grade for strength of concrete is not greater than C50, the 1.0 and 0.8 may be taken for $\alpha_1$ and $\beta_1$ respectively, when the grade for strength of concrete is C80, the 0.94 and 0.74 may be taken for $\alpha_1$ and $\beta_1$ respectively. The values between C50 and C80 may be determined by the linear interpolation method;

$f_c$ – compressive strength of concrete;

$f_y, f'_y$ – tensile strength, compressive strength of steel reinforcements;

$f_a, f'_s$ – tensile strength, compressive strength of encased steel;

$\sigma_s$ – stress of longitudinal bars in the tensile zone;

$\sigma_a$ – stress of flange of encased steel in the tensile zone;

$A_s$, $A'_s$, $A_{af}$, $A'_{af}$ – sectional area of total longitudinal steel reinforcement in tensile zone, in compression zone respectively; sectional area of flange of encased steel in tensile zone, in compression zone respectively;

$a_s$, $a'_s$ – the distance of resultant force point of longitudinal steel reinforcement in tensile zone, in compression zone respectively to the closer section edge;

$a'_a$ – distance of centre of gravity of encased steel flange in compression zone to the closer section edge;

$b$ – width of rectangular section;

$h$ – depth of section;

$h_0$ – effective depth of section, shall be calculated according to the following equation

$$h_0 = \frac{f_a A_{af}\left(\delta_2 h_0 + 0.5 t_{af}\right) + f_y A_s\left(h - a_s\right)}{f_a A_{af} + f_y A_s}$$

$x$ – depth of concrete compression zone;

$\xi$ – relative depth of compression zone, $\xi = x / h_0$;

$\xi_b$ – relative depth of limiting compression zone, $\xi_b = \frac{\beta_1}{1 + \frac{f_y + f_a}{2 \times 0.003 E_s}}$;

$E_s$ – modulus of elasticity of steel;

Other parameters are demonstrated in Fig. 7.

### *4.2 M-N curves*

Based on the calculation method suggested above, the flexural and axial compressive strength (*M-N*) curves of the test specimens can be obtained, as shown in Fig. 8. The maximum flexural

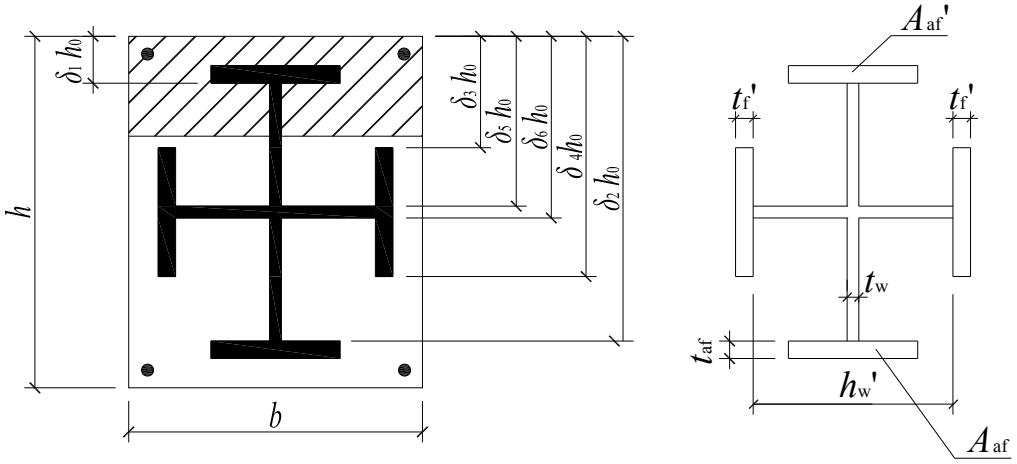


Fig. 7 Cross section of eccentric compression columns

strengths of the test members are also given in Fig. 8. In the figure, second-order effect has been considered.

In Fig. 8, curve 1 is the *M*-*N* relationship of the test specimen in yield state, that is, the yield strengths of steel reinforcement and encased steel are applied when calculated. The Ultimate strengths of steel reinforcement and encased steel are adopted in the calculation of curve 2. The axial compressive strengths of concrete used in the members come from the values of the measured concrete cubes. The confinement effect of the transverse reinforcement on the core concrete is not considered in Fig. 8.

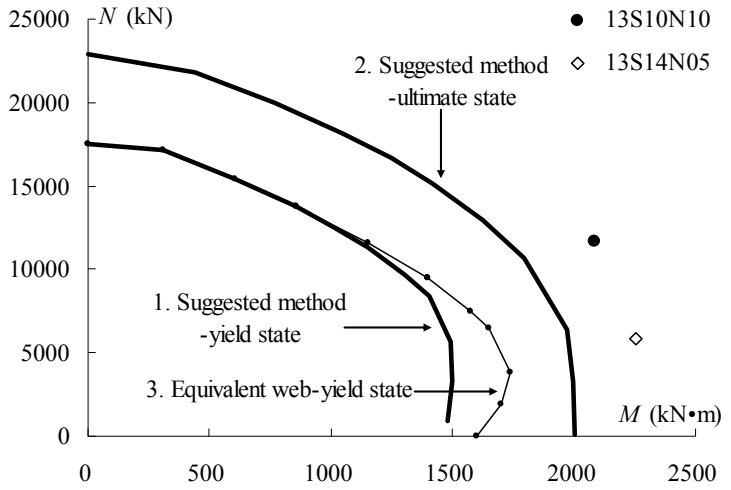


(a) *M*-*N* curves of specimens with 13.12% encased steel ratio

Fig. 8 *M*-*N* curves of test columns

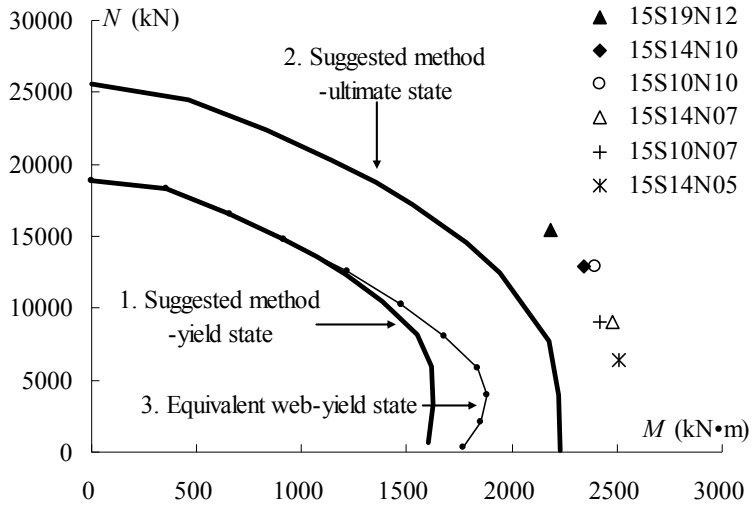


(b) *M*-*N* curves of specimens with 15.04% encased steel ratio

Fig. 8 Continued

Table 4 Comparison of maximum flexural strength ($M_{max}$) between test result and calculation

| Specimen designation | $N_t$ (kN) | Calculational $M_{max}$ (kN·m) | Test $M_{max}$ (kN·m) | Test $M_{max}$ / Calculational $M_{max}$ |
|---|---|---|---|---|
| 13S10N10 | 11634 | 1979 | 2087 | 1.055 |
| 13S14N05 | 5817 | 2176 | 2257 | 1.037 |
| 15S10N07 | 9005 | 2334 | 2434 | 1.043 |
| 15S10N10 | 12864 | 2162 | 2411 | 1.115 |
| 15S14N05 | 6432 | 2397 | 2523 | 1.053 |
| 15S14N07 | 9005 | 2364 | 2494 | 1.055 |
| 15S14N10 | 12864 | 2201 | 2354 | 1.070 |
| 15S19N12 | 15437 | 2148 | 2193 | 1.021 |
| SRC1 (Chen *et al*. 2009) | 1993 | 405 | 426 | 1.052 |
| SRC2a (Chen *et al*. 2009) | 1993 | 398 | 379 | 0.952 |
| SRC2b (Chen *et al*. 2009) | 1993 | 398 | 433 | 1.088 |
| SRC3a (Chen *et al*. 2009) | 1993 | 393 | 376 | 0.957 |
| SRC3b (Chen *et al*. 2009) | 1993 | 392 | 424 | 1.082 |
| SRC4a (Chen *et al*. 2009) | 1993 | 388 | 387 | 0.997 |
| SRC4b (Chen *et al*. 2009) | 1993 | 387 | 414 | 1.070 |
| SRC5 (Chen *et al*. 2009) | 1993 | 383 | 406 | 1.060 |
| Z10-65R (Wang *et al*. 2010) | 3990 | 366 | 416 | 1.137 |
| Z15-65R (Wang *et al*. 2010) | 4350 | 473 | 473 | 1.000 |
| Z15-80R (Wang *et al*. 2010) | 5210 | 416 | 457 | 1.099 |
| Z15-65RS (Wang *et al*. 2010) | 4350 | 465 | 493 | 1.060 |
| Z20-65R (Wang *et al*. 2010) | 4600 | 528 | 596 | 1.129 |

Fig. 8 also shows that the shape of curve 2 is similar to the trend of test results that the maximum flexural strength gradually decreases with increased axial load. The test results are higher than the calculational results which use the ultimate strengths of steel reinforcement and encased steel.

The method of equivalent web is also adopted in calculating the *M-N* curve in Fig.8 (curve 3). Flexural strength calculation of equivalent web method is based on that of the concrete-encased H-shaped steel composite column. That is, $N_{aw2} = N_{aw3} = 0$, $M_{aw2} = M_{aw3} = 0$ in the above suggested formulas. In calculation, the equivalent width $t'_w$ of web is used. The equivalent width is given by

$$t'_w = t_w + \frac{A_{aw} + \sum A'_{af}}{(\delta_2 - \delta_1)h_0} \tag{17}$$

Here, $A'_{aw}$ is the area of horizontal web of encased steel

$\sum A'_{af}$ is the total area of the side flanges of encased steel.

As shown in Fig. 8, when the test axial load ratio is large than 0.8, curve 1 and curve 3 overlap. The smaller the axial load ratio, the larger result difference exists between the two calculational methods. Therefore, within the scope of common axial load ratio ($n_t < 0.6$), if the equivalent web method is adopted in calculating the flexural strength of concrete-encased cross-shaped steel composite column, the results are not safe.

According to the proposed method, Table 4 presents the comparison of maximum flexural strength between experimental results and calculational results of the test specimens in this paper and in references. In the calculation, the confinement effect of the transverse reinforcement on the core concrete is considered; the strengths of confined concrete are obtained based on the theoretical model in reference (Mander *et al*. 1988); the ultimate strengths of steel reinforcement and encased steel are used. In table 4, all the specimens of references and of this paper are concrete-encased cross-shaped steel composite columns with a square cross section; the Q235 steel whose design yield stress is 235 MPa was used in the specimens, and the shear span ratios rang from 3.0 to 3.3, while the encased steel ratios are between 0.4%~20%; all the specimens were tested under uniaxial bending moment and constant axial compressive load; cantilever beam tests were improved and flexural failures occurred. The test maximum flexural strength shown in the table has considered the second-order effect as well.

The comparison in Table 4 shows that: when considering the confinement effect of the transverse reinforcement, the calculational results employing the suggested method are close to the test results. An acceptable predictability of the maximum flexural strength of SRC columns can be obtained by using the proposed formulas.

## 5. Conclusions

In this paper, 8 SRC columns with the encased steel ratio of 13.12% and 15.04% and the test axial load ratio of 0.33-0.80 were tested under the low-frequency cyclic lateral loading. Experimental phenomena are described. The ductility capacity and the maximum strength are discussed. The results show that all the specimens demonstrated good energy dissipation capacity under the cyclic loading. The ductility capacity and maximum strength are highly affected by the level of the axial load ratio as well as the encased steel ratio. The calculation method of flexural strength is suggested. Through considering the confinement effect of the transverse reinforcement

on the core concrete, the computed results are close to the test maximum flexural strength. The proposed calculation method can be used as the acceptable prediction of the maximum flexural strength of SRC columns.

## Acknowledgments

The authors acknowledge the financial support by Grant of Key Project of National Natural Science Foundation of China (90815029); Projects of International Cooperation and Exchanges NSFC (51021140006).

## References

Boyd, P.F., Cofer, W.F. and McLean, D.I. (1995), "Seismic performance of steel-encased composite columns under flexural bending", *ACI Struct. J.*, **92**(3), 335-364.

Chen, C.C., Li, J.M. and Weng, C.C. (2005), "Experimental behaviour and strength of concrete-encased composite beam-columns with T-shaped steel section under cyclic loading", *J. Constr. Steel Res.*, **61**(7), 863-881.

Chen, X.A., Mu, Z.G. and Zhang, J.B. (2009), "Experimental study on the seismic behavior of steel reinforced concrete columns", *J. Univ. Sci. Technol. B.*, **31**(12), 1516-1524. [In Chinese]

Elghazouli, A.Y. and Dowling, P.J. (1992), "Behaviour of composite members subjected to earthquake loading", *Proceedings of the 10th World Conference*, Balkema, Rotterdam, Netherlands, pp. 2621-2626.

GB 50010-2010 (2010), *Code for Design of Concrete Structure*, China Architecture and Building Press, Beijing, China. [English version]

Hajjar, J.F. (2002), "Composite steel and concrete structural systems for seismic engineering", *J. Constr. Steel Res.*, **58**(5), 702-723.

Mander, J.B., Priestley, M.J.N. and Park, R. (1988), "Theoretical stress-strain model for confined concrete", *J. Struct. Eng. – ASCE*, **114**(8), 1804-1826.

Mirza, S., Hyttynen, V. and Hyttinen, E. (1996), "Physical test and analyses of composite steel-concrete beam-columns", *J. Struct. Eng. – ASCE*, **122**(11), 1317-1326.

Plumier, A. and Doneux, C. (2001), *Seismic Behaviour and Design of Composite Steel Concrete Structures*, LNEC Edition, Lisbon, Portugal.

Sav, V., Campian, C. and Senila, M. (2011), "Composite steel-concrete columns with high strength concrete versus normal strength concrete", *Civil Eng. Arch.*, **54**(1), 74-81.

Wang, Y.C. (1999), "Tests on slender composite columns", *J. Constr. Steel Res.*, **49**(1), 25-41.

Wang, H.H., Chen, Y.Y. and Zhao, X.Z. (2010), "Experimental study on SRC columns with high rate of encased steel and their restoring force model", *Earthq. Eng. Eng. Vib.*, **30**(4), 57-65. [In Chinese]

Weng, C.C., Wang, J.C., Liang, C.Y. and Yin, Y.L. (2008), "Seismic cyclic loading test of SRC columns confined with 5-spirals", *Science in China*, *Series E*: *Technological Sciences*, **51**(5), 529-555.

Zhang, S.A., Zhao, Z.Z. and He, X.Q. (2012), "Flexural behavior of SRC columns under axial and bilateral loading", *Appl. Mech. Mater.*, **166**, 3383-3390.

Zheng, S.S., Lou, H.J., Wang, X.F. and Li, Z.Q. (2012), "Study on displacement ductility coefficient of steel reinforced high-strength concrete column", *Adv. Mater. Res*, **368**, 1097-1100.

*CC*